Journal of
Materials Chemistry A

PAPER

View Article Online
View Journal | View Issue

Cite this: J. Mater. Chem. A, 2018, 6, 7053

Ultrafast synthesis of amorphous VO_x embedded into 3D strutted amorphous carbon frameworks–short-range order in dual-amorphous composites boosts lithium storage†

Haoyang Wu,[a] Mingli Qin,*[a] Wei Wang,*[b] Zhiqin Cao,[c] Zhiwei Liu,[a] Qiyao Yu,[d]
Chengyen Lao,[b] Deyin Zhang,[a] Baorui Jia,[a] Donglin He,[a] Tingting Liu,[a]
Alex A. Volinsky,[e] Peng Cao[f] and Xuanhui Qu[a]

Crystalline vanadium oxides have some unique advantages, including abundant material sources, high energy density, and a typical layered structure, making them promising anode candidates for lithium-ion batteries. However, the intrinsic low electrical conductivity and volume expansion side effects severely limit their capacity and cyclability at high charge/discharge rates. Herein, unique dual-amorphous composites with 3D strutted amorphous carbon sheet framework encapsulated amorphous vanadium oxide particles have been prepared by an ultrafast (within one minute), ultralow temperature (172 °C), one-step and large-scale combustion synthesis method. We demonstrate that the dual-amorphous VO_x/C composites provide a large number of accessible active sites and defects for lithium ion intercalation/deintercalation and are self-accommodative to tolerate volume expansion. Another noteworthy point is the short-range ordered atomic arrangement observed in amorphous VO_x that exhibits a larger interlayer spacing ($d_{(001)}$ = 4.80 Å) than other crystalline vanadium oxides. This particular structure has the potential to accommodate more lithium ions and tolerate the volume expansion. Meanwhile the 3D hierarchical porous sheet-like structure facilitates the transfer of electrons and lithium ions. The electrochemical measurements show excellent lithium storage performance with high capacity, good rate capability and long-term cycling stability of the composites.

Received 21st January 2018
Accepted 17th March 2018

DOI: 10.1039/c8ta00654g

rsc.li/materials-a

Introduction

Lithium-ion batteries (LIBs) have been extensively applied in consumer electronics and hybrid electric vehicles.[1–4] A current paradigm shift to large-scale energy storage devices has intensified the global research interest in developing LIBs with excellent reversible capacity, rate capability and long cycling lifetime.[5–8] To meet these demands, a variety of metal oxides (MO_x, M: V, Ti, Fe, *etc.*) have been explored as anode materials for LIBs.[4,5,8] Among them, vanadium oxides have some unique advantages making them promising candidates as anode materials for LIBs, including but not limited to their layered crystal structure, abundant material sources[9] and high energy density.[10,11]

In crystalline metal oxides, a large number of crystallographic sites are accessible for lithium ions. However, the lattice can easily transform into more stable phases after lithium ions occupy these sites causing lithium ions to get permanently trapped inside the lattice, leading to poor reversible capacity.[12] Moreover, the intrinsic low electrical conductivity limits the capacity performance at high charge/discharge rates.[3,13] Three approaches have been considered in order to solve the aforementioned drawbacks. One way is to synthesize amorphous metal oxides.[14–16] Research studies[17,18] show that the defects in an amorphous structure can serve as storage sites for reversible lithium ions, contributing to a high capacity. A second approach is to incorporate amorphous carbon into oxides to form crystallized metal oxide/amorphous carbon composites, as amorphous carbon provides a cushion layer and a conductive pathway and therefore facilitates the transfer of electrons.[19,20] The third approach is to engineer a three-

---

[a] *Institute for Advanced Materials and Technology, University of Science and Technology Beijing, Beijing 100083, China. E-mail: qinml@mater.ustb.edu.cn*

[b] *Department of Materials Science and Metallurgy, University of Cambridge, Cambridge CB3 0FS, UK. E-mail: wwang_bj@126.com*

[c] *School of Materials Science and Engineering, Panzhihua University, Panzhihua 617000, China*

[d] *Department of Applied Chemistry, Harbin Institute of Technology, Harbin 150001, China*

[e] *Department of Mechanical Engineering, University of South Florida, E. Fowler Ave., ENB118, Tampa, FL 33620, USA*

[f] *Department of Chemical and Materials Engineering, University of Auckland, Private Bag 92019, Auckland 1142, New Zealand*

† Electronic supplementary information (ESI) available. See DOI: 10.1039/c8ta00654g

dimensional (3D) porous structure. The 3D porous structure could provide a shortened and efficient diffusion path for electrons and lithium ions, leading to good conductivity and fast charge/discharge rates.[21,22] Despite the above modification, the synthetic process is usually carried out under an inert atmosphere and needs a long time.

In this study, we combined the above approaches to design dual-amorphous composites with a unique hierarchical and porous structure through encapsulating amorphous vanadium oxide particles into 3D strutted amorphous carbon sheet frameworks. The amorphous VO_x possesses a larger interlayer spacing in short-range order that can potentially accommodate more lithium ions and endure the volume expansion. In addition, the 3D hierarchical and porous sheet-like structure can facilitate the transfer of lithium ions and electrons. The assembly of the dual-amorphous composites is achieved *via* an ultrafast (within one minute), ultralow temperature (172 °C), one-step and large-scale solution combustion synthesis (SCS) technique.

Essentially, the SCS process is a self-sustained and exothermal redox reaction between oxidizers and fuels.[23,24] The process can be fulfilled in an ambient environment within only a few minutes. During the redox process, ammonium metavanadate transforms into vanadium oxide particles accompanied by the carbonization of glucose. The ultralow temperature and ultrafast reaction time result in the formation of a dual-amorphous structure with defects. The released gas produces pores in the vanadium oxides/carbon composites, resulting in the formation of 3D hierarchical and porous sheet structures. The as-synthesized amorphous vanadium oxides/amorphous carbon composites display good cycling behavior with a high reversible capacity of 1088 mA h g^{-1} at 0.1 A g^{-1} after 100 cycles and 776 mA h g^{-1} at 1 A g^{-1} after 300 cycles. This work highlights the importance of dual-amorphous vanadium oxides/carbon composites with short-range order as good alternative anodes in enhancing the capacity, rate capability, and stability of LIBs. Moreover, the one-step SCS technique has the potential to be scaled up and is time- and energy-efficient and cost-effective, and can be utilized as a general approach for fabricating other dual-amorphous composites for numerous applications such as batteries, supercapacitors and electrocatalysts.

Experimental details

Materials synthesis

The starting reactants were 0.05 mol ammonium metavanadate (NH_4VO_3), 0.4 mol ammonium nitrate (NH_4NO_3), 0.04 mol glycine ($C_2H_5NO_2$), 0.16 mol citric acid ($C_6H_8O_7$) and appropriate amounts of glucose ($C_6H_{12}O_6$). The reactants were first dissolved in DI water in a 500 mL beaker followed by thorough stirring to form a homogeneous precursor solution. The precursor solution was then heat treated in an electrical furnace in air. Once the majority of the water was evaporated and the solution became a sticky paste, an instantaneous combustion occurred. The combustion process only took less than one minute and a foamy product was synthesized. For the sake of simplicity, the as-prepared vanadium oxides/carbon composites are hereafter designated as VO_x/nC, where n is the molar ratio of glucose and ammonium metavanadate ($n = 0.1$, 0.2 and 1). For comparison, we selected the $VO_x/0.2C$ sample for further annealing at 400 °C in air for 1 h. This annealed sample is hereafter denoted as VO_x/0.2C-400. Moreover, the carbon synthesized by the SCS method (denoted as pyrolytic carbon) was also prepared by identical procedures except for the absence of NH_4VO_3.

Materials characterization

X-ray powder diffraction (XRD) was used to detect the phase constituents of the samples using a Rigaku D/max-RB12 diffractometer with Cu Kα radiation. The morphology of the products was characterized by scanning electron microscopy (SEM, JEOL, JSM-7001F). A transmission electron microscope (JEOL, JEM-2010) was used to obtain transmission electron microscopy (TEM) images and energy dispersive X-ray spectra (EDS). The thermal behavior of the formed gels was identified by differential scanning calorimetry (DSC) and thermal gravimetry (TG) using an STA-449F3 thermal analyzer in a temperature range of 25–400 °C at a ramp rate of 10 °C min^{-1} in air. The surface chemistry was characterized by X-ray photoelectron spectrometry (XPS) (ESCALAB 250, PerkinElmer). Fourier transform infrared (FTIR) absorption spectra of the samples were recorded with a NEXUS-670 IR spectrometer of 4 cm^{-1} resolution, over a wavelength range of 400–4000 cm^{-1}. The Brunauer–Emmett–Teller (BET) method was used to determine the specific surface area of the products using an Automated Surface Area & Pore Size Analyzer (QUADRASORB SI-MP, Quantachrome Instruments, Boynton Beach, FL). A microscopic confocal Raman spectrometer (Renishaw RM2000) was used to obtain Raman spectra at an excitation wavelength of 514.5 nm. The contents of carbon in the VO_x/nC samples were measured with a LECO CS844 analyzer. The content of nitrogen in the VO_x/0.2C sample was measured with an elemental analyzer (MICRO CORDER JM10, J-SCIENCE LAB).

Electrochemical measurements

Electrochemical measurements were performed in CR2023-type coin cells. The active materials, acetylene black and polyvinylidene fluoride (PVDF) were mixed in a weight ratio of 60 : 30 : 10. The mixture was made into a slurry with *N*-methylpyrrolidone that was later doctor bladed uniformly on Cu foil. These prepared electrode sheets were vacuum-dried at 60 °C for 12 h and pressed at 10 MPa. The electrolyte was 1 M $LiPF_6$ in 1 : 1 ethylene carbonate (EC) and dimethyl carbonate (DMC). The counter electrode was lithium metal. The half cells were galvanostatically charged and discharged between 0.01 and 3 V at two different rates: 1 A g^{-1} and 0.1 A g^{-1}. For the rate testing, the charge/discharge current was gradually increased from 0.1 A g^{-1} to 0.2, 0.5, 1, 2, 5 and 10 A g^{-1}, and then decreased to 1 A g^{-1} step by step. An electrochemical workstation (CHI618D) was used to collect cyclic voltammetry (CV) curves at 0.1 mV s^{-1} in the range of 0.01–3.0 V.

Results and discussion

Fig. 1a shows a schematic diagram of the solution combustion synthesis procedure. Firstly, all raw materials were mixed at the molecular level in the precursor solution to achieve a homogenous phase distribution in the product. The precursor solution had a saffron yellow color (Fig. 1b). As the complex compound was formed, the color of the solution changed to tawny. Upon heating, partial V^{5+} was reduced to V^{4+} by the reductant and a blue gel was formed. Once ignited, the exothermic reaction between the oxidizer (NH_4NO_3) and fuel ($C_2H_5NO_2$ and $C_6H_8O_7$) provides the energy required for sustaining the combustion reaction without an additional thermal energy input. More importantly, the whole mild combustion process only takes less than one minute. During the process, ammonium metavanadate transforms into VO_x particles, which are homogeneously distributed in the 3D hierarchical and porous carbon sheets generated from the *in situ* carbonization of glucose.

The TG-DSC curves of the formed VO_x/0.2C gel are recorded, which was obtained by evaporating a part of water at 100 °C (Fig. 1c). The gel sample undergoes a mass loss of ~20% before 110 °C, due to the residual water evaporation. A sharp exothermic peak appears at approximately 172 °C, concomitant with a large mass loss of ~60%. At this temperature, the combustion is ignited and an excessive heat is released. The released heat causes glucose decomposition and carbonization,[25–27] and the residual heat is insufficient to crystallize the vanadium oxides and carbon. As a result, vanadium oxides/carbon composites with a dual-amorphous structure are formed.

Fig. 1d compares the XRD patterns of the four samples. The VO_x/0.1C sample only shows a sharp peak at $2\theta = 26.1°$, which can be indexed to V_2O_5. This suggests that the VO_x/0.1C sample is not well-crystallized and consists of small nanocrystals, owing to the low amount of glucose addition. In the case of VO_x/0.2C and VO_x/1C samples, the XRD patterns do not show any obvious Bragg diffraction peaks, indicating their amorphous nature. When the VO_x/0.2C powder was annealed at 400 °C, a well-crystallized orthorhombic V_2O_5 phase is obtained, as per JCPDS 89-0612.

The FTIR spectra of these samples are shown in Fig. 1e. The peak position of the vanadyl mode (V–O) is at 1017 cm^{-1} for the annealed VO_x/0.2C-400 sample.[27] In other samples, this mode is located at ~977 cm^{-1},[26] which is in agreement with poorly crystallized and amorphous VO_x.[28,29] Bands at 3400 and 1650 cm^{-1} are attributed to different vibrational modes of the

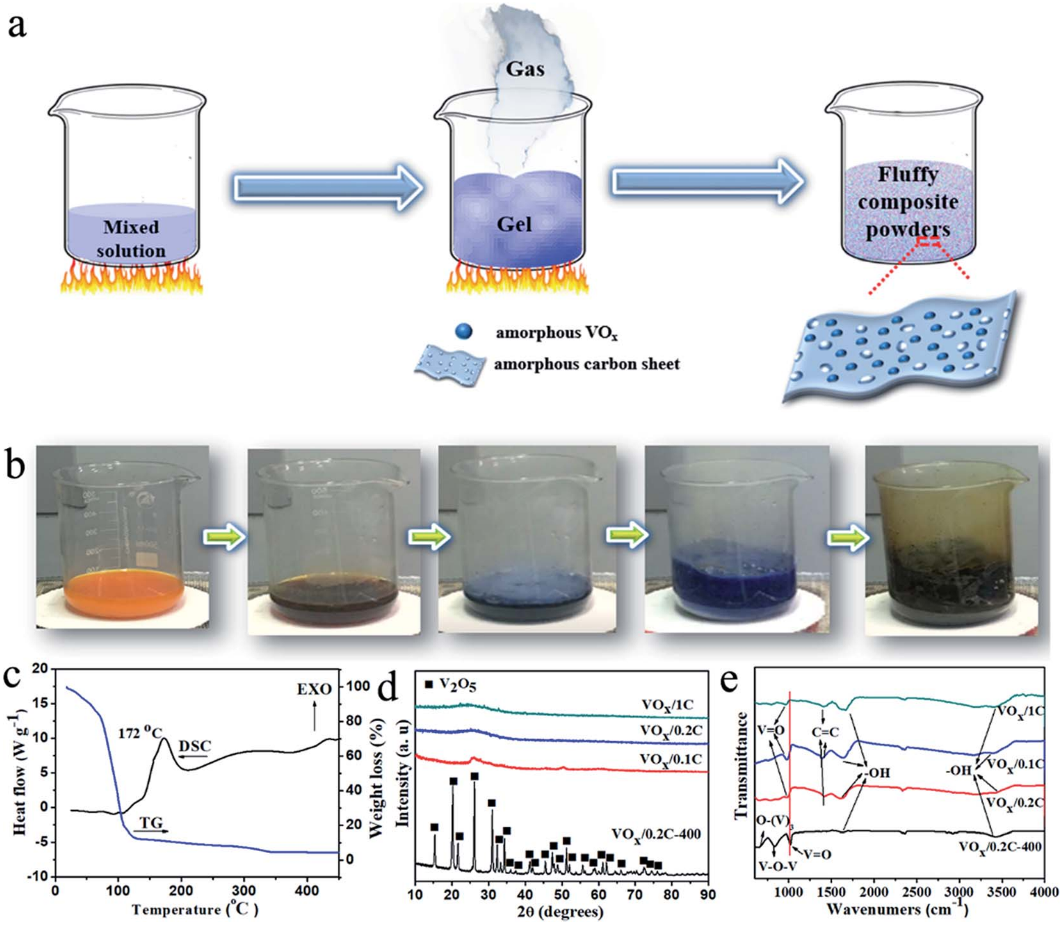

Fig. 1 (a) Schematic illustration of the porous VO_x/*n*C sheet fabrication process. (b) Photos of the reaction process. (c) TG and DSC curves of the gelatinous mass of VO_x/0.2C. (d) The XRD patterns and (e) the FTIR spectra of the four samples.

O–H group of adsorbed water molecules.[30] The IR active mode located at 820 cm^{-1} is characteristic of C=C vibrations,[17] which are not shown in the VO$_x$/0.2C-400 sample.

Fig. 2a–d show typical SEM images of the four products. The VO$_x$/0.1C (Fig. 2a) sample exhibits a sheet-like structure in which there are some little fragments. As displayed in Fig. 2b, the VO$_x$/0.2C sample has a 3D porous sheet architecture. Obviously, the 3D sheet architecture consists of pores with different sizes in the range of 70 to 200 nm. With higher glucose content, the VO$_x$/1C sample shares a similar sheet-like morphology with VO$_x$/0.2C, but the sheets are rather dense and compact and there are no pores (Fig. 2c). The differences in the morphology of the three samples can be attributed to the glucose additive content. The redox combustion reaction between oxidants and fuels releases a lot of gases, resulting in the formation of pores in the sheet structure.[31–34] The growth of pores would be inhibited by the carbon generated from the *in situ* carbonization of glucose. However, too small amounts of the carbon could not sufficiently exert the inhibiting effect, on the other hand too much would restrain the pore formation.[32–35] As measured using the Leco analyzer, the carbon content in the VO$_x$/0.1C, VO$_x$/0.2C and VO$_x$/1C samples is 7 wt%, 14 wt% and 30 wt%, respectively (Table S1†). In comparison, the VO$_x$/0.2C-400 sample, which was annealed in air at 400 °C, maintains the porous sheet architecture (Fig. 2d and S1†). Inside the porous architecture are uniformly distributed nano-sized V$_2$O$_5$ particles of 200 nm. It is noted that the VO$_x$ particles are uniformly distributed in the VO$_x$/0.2C sheet architecture, and the majority of the particles are interconnected, forming a porous freestanding sheet structure even after the carbon content is removed.

The representative TEM images of the VO$_x$/0.2C sample are presented in Fig. 2e and f. The low-magnification TEM image clearly shows the hierarchical and porous sheet structure (Fig. 2e). In regard to its amorphous nature, the high-resolution TEM (HRTEM) image does not show any crystalline lattice fringes which is consistent with the XRD (Fig. 1d) and SAED results (see the inset of Fig. 2f). EDS elemental mapping results clearly reveal that the elements V, O and C are evenly distributed throughout the VO$_x$/0.2C sample (Fig. 2g–j). The BET surface area of the VO$_x$/0.2C sample is determined to be 20.99 m^2 g^{-1}, higher than that of the VO$_x$/0.1C (5.26 m^2 g^{-1}) sample. The average pore sizes of VO$_x$/0.2C and VO$_x$/0.1C samples are 41.97 nm and 10.01 nm, respectively, belonging to mesopores, which could effectively increase the electrode/electrolyte contact area and shorten the path length for ionic/electronic transport. On further increasing the content of glucose additive, the VO$_x$/1C sample exhibits a BET surface area of 6.68 m^2 g^{-1} with an average pore size of 20.90 nm, smaller than that of the VO$_x$/0.2C sample.

To reveal the valence states of vanadium in the four products, XPS measurements were performed. The binding energies obtained in the XPS analysis are corrected for specimen charging by referencing C 1s to 284.81 eV. Fig. S2† reveals the XPS survey spectrum of VO$_x$/0.2C, which mainly consists of C, V, O and N elements. Fig. S3† presents the N 1s XPS spectra. The peak at 399.5 eV corresponds to pyrrolic-N, confirming the presence of doped N atoms in the carbon sheet structure,[36] and

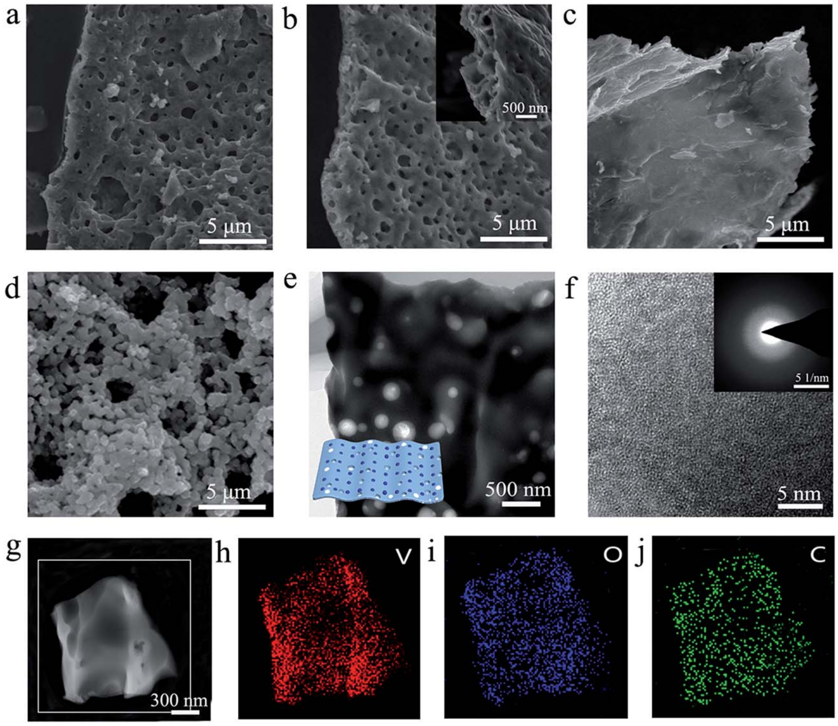

Fig. 2 SEM images of the four samples: (a) VO$_x$/0.1C, (b)VO$_x$/0.2C, (c) VO$_x$/1C and (d)VO$_x$/0.2C-400, the inset of (b) is the enlarged SEM image. TEM (e) and HRTEM (f) images and EDS elemental mapping (g–j) of the VO$_x$/0.2C sample, the inset of (f) is the corresponding SAED pattern.

the N-doping content is determined to be 3 wt%. The presence of N atoms on the carbon surface could enhance the electrical conductivity and facilitate lithium ion and electron diffusion.[37]

Fig. S4a† reveals a fitted high-resolution XPS spectrum of V 2p. The V $2p_{3/2}$ peak is fitted into two peaks of 516.4 eV for V^{4+} and 517.2 eV for V^{5+}, whereas the V $2p_{1/2}$ peak is fitted into two peaks of 523.6 eV for V^{4+} and 524.8 eV for V^{5+}. The valence states of vanadium in VO_x/0.1C and VO_x/1C are similar to that of VO_x/0.2C(Fig. S4b and c†). For VO_x/0.2C-400, the fitted V $2p_{3/2}$ and V $2p_{1/2}$ peaks observed at 517.2 and 524.8 eV correspond to V^{5+}. Furthermore, Raman spectroscopy is used for characterizing carbon in the VO_x/0.2C composite. As shown in Fig. S5,† two peaks at 1389 and 1569 cm^{-1} can be characterized by the D and G bands, respectively. The Raman spectrum of VO_x/0.2C shows that the D-band (assigned to the A_{1g} vibration mode of sp^2 carbon rings caused by defects) is more intense than the G-band (assigned to the E_{2g} vibration mode of sp^2 carbon atoms) ($I_D/I_G = 1.41$), indicating its amorphous nature.

The lithium-storage performances of the as-prepared four powders as anodes were evaluated. The cyclic voltammetry (CV) curves of the three VO_x/nC samples are similar (Fig. 3a, S6a and S7a†). In the first cycle, only one discernible cathodic peak is observed, which is ascribed to the formation of Li_yVO_x new phases and a solid-electrolyte interphase (SEI) layer on the surface of the active materials.[17,38,39] From the second cycle onwards, the peak positions of the VO_x/0.2C sample have a slight shift. The possible reasons could be the activation process and the formation of the SEI layer.[17,38,40] In addition, the CV curves are nearly unchanged from the fourth cycle onwards, indicating good charging and discharging reversibility. For comparison, the VO_x/0.2C-400 sample was also subjected to CV assessment (Fig. S8a†). Unlike the unannealed sample, the annealed VO_x/0.2C-400 demonstrates two cathodic peaks at 0.26 and 1.6 V in its first CV cycle, corresponding to the successive lithium intercalation into V_2O_5 to form various $Li_yV_2O_5$ phases.[10] Fig. 3b and S8b† compare the charge/discharge profiles of the VO_x/0.2C and VO_x/0.2C-400 samples at 0.1 Ag^{-1} from the first to the sixth cycle. All the voltage plateaus in the discharge/charge curves match well with the CV peaks with no obvious change observed in subsequent cycles, indicating reversible intercalation/deintercalation reactions. The charge/discharge profiles for the other samples are presented in Fig. S6b and S7b.† It is worth mentioning that the unannealed VO_x/0.2C shows a higher specific capacity than the annealed counterpart.

Fig. 3c displays the cycling performance of the four samples at 0.1 A g^{-1}. Apparently, the VO_x/0.2C electrode exhibits a much higher reversible capacity than the other three electrodes. The reversible capacity is 1010 mA h g^{-1} after 52 cycles and 1088 mA h g^{-1} after 100 cycles. Furthermore, the coulombic efficiency rapidly increases from 65% to 98% in the first six cycles and remains nearly 100% in subsequent cycles. Under the same testing conditions, the other three samples, however, have a far lower capacity than the VO_x/0.2C sample. For instance, after 100 cycles, the VO_x/0.1C, VO_x/1C and VO_x/0.2C-400 samples only achieve a reversible capacity of 792 mA h g^{-1}, 354 mA h g^{-1} and 713 mA h g^{-1} respectively.

Fig. 3d displays the rate performances of the four electrodes. Again, the VO_x/0.2C electrode delivers the best performance: reversible capacities of 690, 632, 580, 552 and 320 mA h g^{-1} are observed after a step wise increase of the charge and discharge current densities to 0.1, 0.2, 0.5, 1 and 5 A g^{-1}. Remarkably, after 70 cycles at different current densities, the capacity can be restored to 640 mA h g^{-1} when the current density returns to 1.0 A g^{-1}, indicating the existence of a re-activation process and excellent rate performance and reversibility. In contrast, VO_x/0.1C, VO_x/1C and VO_x/0.2C-400 only exhibit a reversible capacity of approximately 100 mA h g^{-1} at a rate of 5 A g^{-1}. Moreover, when the current density returns to 1 A g^{-1} after 70 cycles at different current densities, the capacity of VO_x/0.1C, VO_x/1C and VO_x/0.2C-400 is only restored to 282, 127 and 243 mA h g^{-1} respectively. Meanwhile, electrochemical impedance spectroscopy (EIS) was performed to further confirm the enhanced lithium-storage performance. In the Nyquist plot, the diameter of the semicircle for the VO_x/0.2C electrode is the smallest among the investigated electrodes (Fig. S9†), indicating the lowest charge-transfer resistance (R_{ct}). Hence, the electron-transfer rate, as well as the rate performance, is improved. The much larger semicircle for the VO_x/0.2–400 sample is attributed to the absence of conducting carbon.

To highlight the superiority of the unique VO_x/0.2C anode material, we tested the cycling performance of the VO_x/0.2C sample at 1 A g^{-1}. Fig. 3e gives the capacity as a function of cycle number between 0.01 and 3 V at 1 A g^{-1} for the VO_x/0.2C sample. It is obvious that the sample delivers a high capacity of 979 mA h g^{-1} in its first discharge, but the capacity fades significantly to 386 mA h g^{-1} in the early 14 cycles (transient stage). The significant irreversible capacity loss at the transient stage may be due to the decomposition of the electrolyte and inevitable formation of the SEI layer, which is common to most anode materials.[41] In subsequent cycles, the reversible capacity increases to 778 mA h g^{-1} at the 230th cycle, and remains stable at approximately 776 mA h g^{-1} up to the 300th cycle with a coulombic efficiency of 99.7%. An increased capacity after a number of cycles has been observed for vanadium oxides and other transition metal oxides, owing to the activation and growth of an electrochemical gel-like polymer layer.[40,42,43] The voltage plateaus in the discharge/charge curves are not obvious, similar to the inconspicuous CV peaks. The phenomenon can be attributed to the amorphous structure of the VO_x/0.2C sample.[17] To investigate the effect of amorphous carbon on the capacity of the VO_x/0.2C sample, we tested the cycle performance of the pyrolytic carbon samples (without any metal oxides) at a current density of 1 A g^{-1} (Fig. S11b†). Although the amorphous carbon electrode exhibits good cycle stability, the capacity is only 298 mA h g^{-1} after 100 cycles. It is evident that the amorphous carbon existing in the VO_x/0.2C composite offers a synergistic effect to promote the capacity and cycle stability of the VO_x/0.2C composite. This phenomenon is similar to other reports.[20,44]

Fig. S12a† shows the V 2p spectra of lithiated and delithiated VO_x/0.2C samples. After lithiation to 0.01 V, the V $2p_{3/2}$ peak is fitted into two peaks of 516.6 eV for V^{4+} and 517.4 eV for V^{5+}, whereas the V $2p_{1/2}$ peak is fitted into two peaks of 523.7 eV for

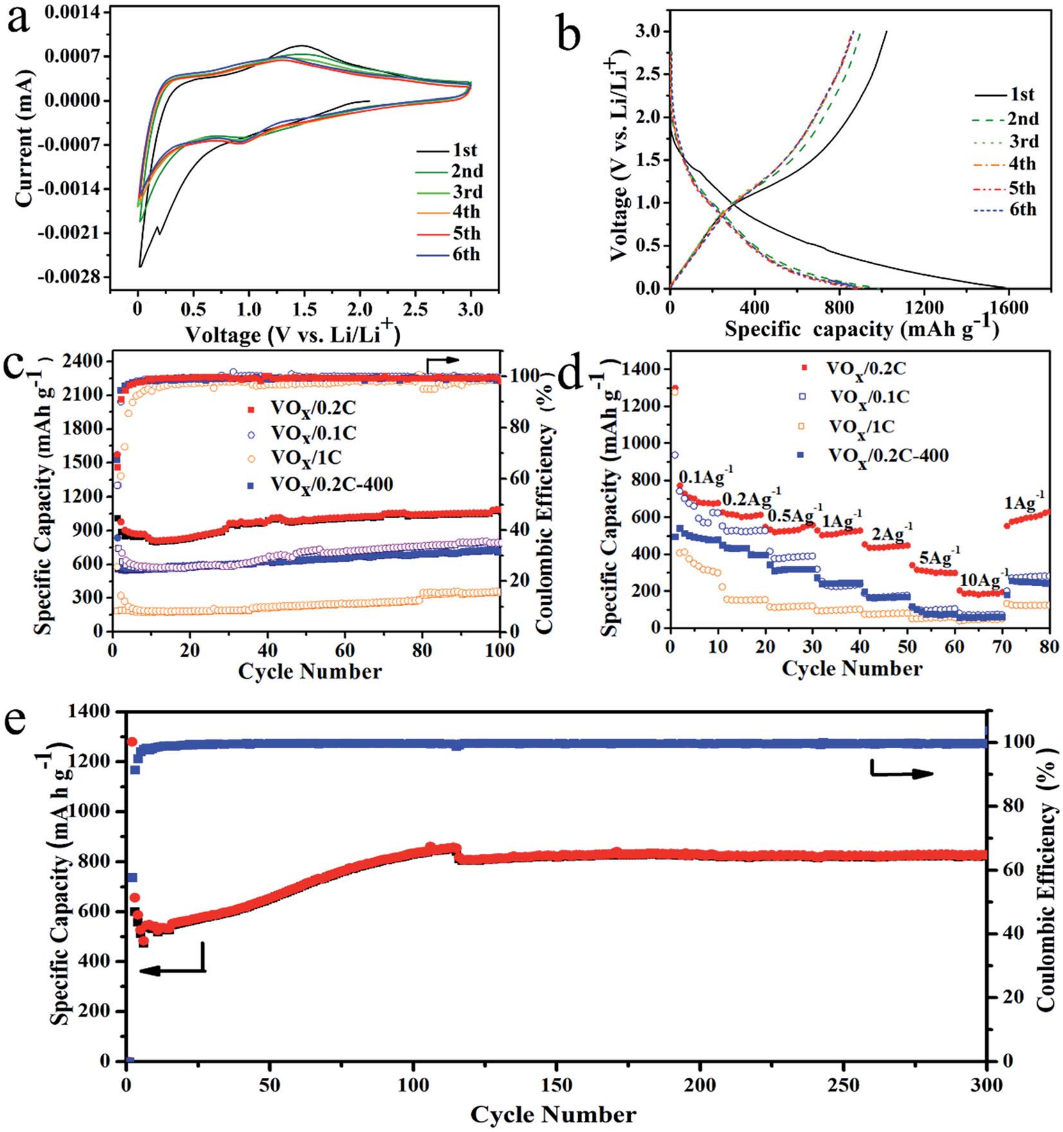

Fig. 3 Electrochemical performance of the samples: (a) CV curves of $VO_x/0.2C$ recorded at 0.1 mV s^{-1} in the range of 0.01 to 3 V *versus* Li/Li^+. (b) The corresponding charge/discharge profiles of $VO_x/0.2C$ at 0.1 A g^{-1}. (c) Comparison of cycling performance of all the samples at 0.1 A g^{-1}. (d) Comparison of charge capacity of all the samples at various rates for 80 cycles. (e) Cycling performance of $VO_x/0.2C$ tested at 1 A g^{-1}.

V^{4+} and 525.0 eV for V^{5+}, indicating the formation of Li_xVO_2 and $Li_xV_2O_5$. After delithiation, the XPS spectrum of V 2p could also be fitted into peaks of V^{4+} and V^{5+}. Moreover, compared with the XPS spectrum of V 2p in the pristine $VO_x/0.2C$ (Fig. S4a†) and its integral area, the binding energies of the electrode delithiated to 3 V shift to higher values and the electrode involves a smaller amount of V^{4+}. This phenomenon is similar to other reports.[17,45] For comparison, the lithiated and delithiated $VO_x/0.2C$-400 samples were also subjected to XPS analysis (Fig. S12b†). After lithiation, the broad peak can be fitted into two peaks of 516.4 eV and 517.4 eV together with V $2p_{1/2}$ at 523.4 eV and 524.6 eV corresponding to V^{4+} and V^{5+} states, respectively, indicating the partial reduction of the V^{5+} state. After delithiation to 3 V, the fitted V $2p_{3/2}$ peak is fitted into two peaks of 516.5 eV for V^{4+} and 517.5 eV for V^{5+}, and the V $2p_{1/2}$ peak is fitted into two peaks of 523.5 eV for V^{4+} and 524.8 eV for V^{5+}. The phenomenon is analogous to that of the $VO_x/0.2C$ sample, indicating a similar charge/discharge process.

In view of the above analysis, it looks that the lithium ion storage mechanisms of crystalline vanadium oxide and $VO_x/0.2C$ are quite different (Fig. 4a and b). For the crystalline vanadium oxide, the lithium ions are trapped inside the lattice after the charging process with an impact of crystalline structural deformation (Fig. 4b) due to the volume expansion, resulting in poor reversible capacity. Apart from the difference in lithiation, the amount of lithium ion uptake is different between $VO_x/0.2C$ and its crystalline counterpart due to interlayer spacing. Although the $VO_x/0.2C$ sample has an amorphous structure, it indeed possesses nominal interlayer spacings in short-range order, which are estimated to be 4.80 Å (Fig. 4c and d). Compared with crystalline V_2O_5 (the interlayer spacing of (001) is 4.38 Å), the interlayer spacings of $VO_x/0.2C$ are much

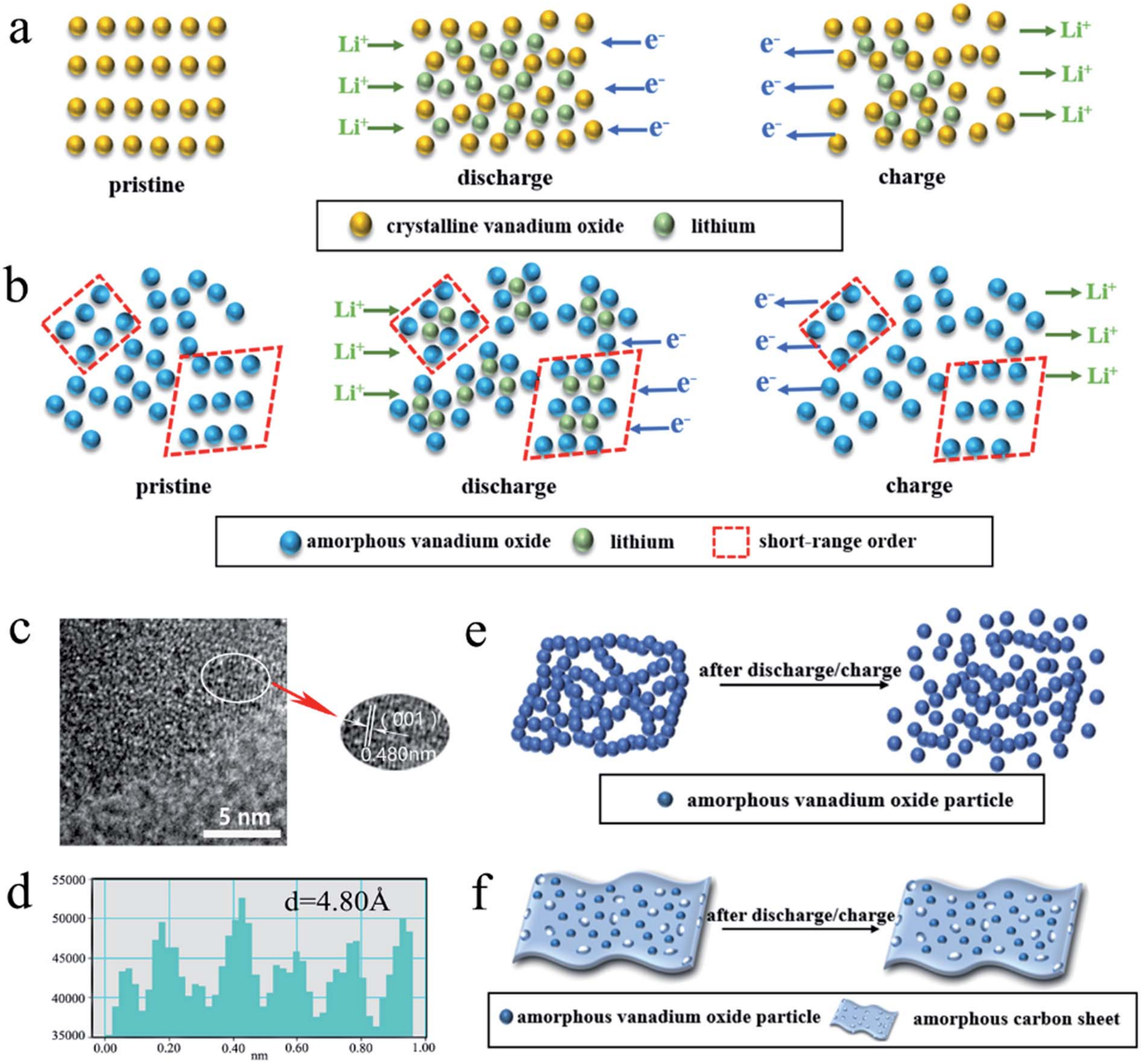

Fig. 4 Schematic illustration of the discharge and charge process of (a) crystalline vanadium oxide and (b) VO_x/0.2C. (c) HRTEM images and (d) the corresponding interlayer spacing of the VO_x/0.2C sample. Schematic illustration of the morphology change process of (e) amorphous vanadium oxide and (f) VO_x/0.2C after the discharge and charge process.

larger. During the discharge and charge process, the structure can accommodate more lithium ions, adapt to the interlayer spacing change and better accommodate the volume expansion, resulting in a battery behavior with high capacity, high rate capability and long cycle life. Moreover, unlike the individual vanadium oxide particles which can agglomerate and collapse during cycling (Fig. 4e), the sheet-like structure of the VO_x/0.2C sample can be still maintained (Fig. S13† and 4f), indicating its structural durability. This can be attributed to the incorporation of the amorphous carbon sheet, which could provide a cushion layer.

Fig. S14† compares our study with vanadium oxide materials reported in the literature. The VO_x/0.2C material here exhibits excellent reversible capacity at the same rate.[10,12,17,43,46–49] The excellent electrochemical performance of the VO_x/0.2C sample could be due to the following reasons: (a) the dual-amorphous structure utilizes the synergistic effect of amorphous VO_x and amorphous carbon. The amorphous carbon sheet could compensate for the low conductivity of the inner VO_x cores, relieve the aggregation and buffer the large volume change of the VO_x nanoparticles, and the amorphous VO_x obtained at ultralow temperature could provide defects and vacancies for fast lithium ion intercalation, similar to other research studies.[17,18] The amorphous carbon sheet together with the VO_x particles can both improve the rate performance and cycle life. Thus the so-called synergistic effects can be obtained. (b) The large interlayer spacing in short-range order in the amorphous structure can accommodate more lithium ions and be self-accommodative to tolerate volume expansion. Indeed, in a well-crystallized structure, the volume will dramatically expand after alkali ion intercalation, while in the short-range-order structure, just a few atoms are arranged orderly, forming a number of small units. These small units are more flexible and adaptable, which can tolerate the volume change during cycling.[50,51] (c) The 3D hierarchical and porous sheet architecture provides a short transport path for both lithium ions and electrons, resulting in fast charge/discharge rates.[52,53] The pores in the sheet structure facilitate the access of electrolyte into the electrode materials and improve the lithium ion kinetics.[54,55] All these factors contribute to the outstanding electrochemical properties of the VO_x/0.2C sample.

Conclusion

In summary, we have successfully synthesized dual-amorphous VO_x/carbon composites (VO_x/0.2C) by an ultrafast (within one minute), ultralow temperature (172 °C), one-step and large-scale solution combustion method. VO_x/0.2C exhibits a hierarchical and porous sheet structure, in which small VO_x particles are encapsulated in the 3D hierarchical and porous carbon sheet support. We demonstrate that the dual-amorphous VO_x/C composites possess a large interlayer spacing in short-range order, which has the potential to accommodate more lithium ions and are self-accommodative to tolerate volume expansion. Meanwhile, the 3D hierarchical and porous sheet-like structure facilitates the transfer of electrons and lithium ions. The VO_x/0.2C electrode exhibits an excellent reversible capacity (1088 mA h g^{-1} at 0.1 A g^{-1} after 100 cycles, and 776 mA h g^{-1} at 1 A g^{-1} after 300 cycles), high coulombic efficiency (∼99%), superior cycling stability and good rate capability. The synthesis process is cost-effective, time-saving and easy to scale up. We envisage that the proposed process has the potential for the large-scale production of dual-amorphous metal oxide/carbon composite electrode materials.

Conflicts of interest

There are no conflicts to declare.

Acknowledgements

This work is financially supported by the Beijing Natural Science Foundation (2184111), the National Natural Science Foundation of China (contract numbers: 51574031, 51574030, 51604240, 51604025 and 51574029), the Natural Science Foundation Program of Beijing (contract no. 2162027), the National 863 Program (2013AA 031101), the China Postdoctoral Science Foundation (2016M591073) and the Fundamental Research Fund for the Central Universities (FRF-TP-17-029A1).

Notes and references

1 A. S. Aricò, P. Bruce, B. Scrosati, J.-M. Tarascon and W. Van Schalkwijk, *Nat. Mater.*, 2005, **4**, 366–377.
2 B. Dunn, H. Kamath and J.-M. Tarascon, *Science*, 2011, **334**, 928–935.
3 P. Poizot, S. Laruelle, S. Grugeon, L. Dupont and J. Tarascon, *Nature*, 2000, **407**, 496–499.
4 P.-L. Taberna, S. Mitra, P. Poizot, P. Simon and J.-M. Tarascon, *Nat. Mater.*, 2006, **5**, 567–573.
5 C. He, S. Wu, N. Zhao, C. Shi, E. Liu and J. Li, *ACS Nano*, 2013, **7**, 4459–4469.
6 N. Rudawski, B. Yates, M. Holzworth, K. Jones, R. Elliman and A. Volinsky, *J. Power Sources*, 2013, **223**, 336–340.
7 N. G. Rudawski, B. L. Darby, B. R. Yates, K. Jones, R. Elliman and A. Volinsky, *Appl. Phys. Lett.*, 2012, **100**, 083111.
8 X. Xin, X. Zhou, J. Wu, X. Yao and Z. Liu, *ACS Nano*, 2012, **6**, 11035–11043.
9 Y. Wang, H. J. Zhang, A. S. Admar, J. Luo, C. C. Wong, A. Borgna and J. Lin, *RSC Adv.*, 2012, **2**, 5748–5753.
10 J. Liu, H. Xia, D. Xue and L. Lu, *J. Am. Chem. Soc.*, 2009, **131**, 12086–12087.
11 Y. Yang, D. Kim, M. Yang and P. Schmuki, *Chem. Commun.*, 2011, **47**, 7746–7748.
12 O. B. Chae, J. Kim, I. Park, H. Jeong, J. H. Ku, J. H. Ryu, K. Kang and S. M. Oh, *Chem. Mater.*, 2014, **26**, 5874–5881.
13 J.-M. Tarascon and M. Armand, *Nature*, 2001, **414**, 359–367.
14 E. Hüger, L. Dörrer, J. Rahn, T. Panzner, J. Stahn, G. Lilienkamp and H. Schmidt, *Nano Lett.*, 2013, **13**, 1237–1244.
15 E. Uchaker, Y. Zheng, S. Li, S. Candelaria, S. Hu and G. Cao, *J. Mater. Chem. A*, 2014, **2**, 18208–18214.
16 X.-L. Wang, W.-Q. Han, H. Chen, J. Bai, T. A. Tyson, X.-Q. Yu, X.-J. Wang and X.-Q. Yang, *J. Am. Chem. Soc.*, 2011, **133**, 20692–20695.
17 D. Zhao, L. Zheng, Y. Xiao, X. Wang and M. Cao, *ChemSusChem*, 2015, **8**, 2212–2222.
18 D. Zhao, J. Qin, L. Zheng and M. Cao, *Chem. Mater.*, 2016, **28**, 4180–4190.
19 X. Liu, J. Zai, B. Li, J. Zou, Z. Ma and X. Qian, *J. Mater. Chem. A*, 2016, **4**, 10552–10557.
20 X. Xu, H. Tan, K. Xi, S. Ding, D. Yu, S. Cheng, G. Yang, X. Peng, A. Fakeeh and R. V. Kumar, *Carbon*, 2015, **84**, 491–499.
21 R. Tian, W. Wang, Y. Huang, H. Duan, Y. Guo, H. Kang, H. Lia and H. Liu, *J. Mater. Chem. A*, 2016, **4**, 13148–13154.
22 X. Xu, K. Cao, Y. Wang and L. Jiao, *J. Mater. Chem. A*, 2016, **4**, 6042–6047.
23 A. Varma, A. S. Mukasyan, A. S. Rogachev and K. V. Manukyan, *Chem. Rev.*, 2016, **116**, 14493–14586.
24 F. Li, J. Ran, M. Jaroniecc and S. Z. Qiao, *Nanoscale*, 2015, **7**, 17590–17610.
25 M. Jayalakshmi and K. Balasubramanian, *Int. J. Electrochem. Sci.*, 2009, **4**, 878–886.
26 M. Jayalakshmi, M. Palaniappa and K. Balasubramanian, *Int. J. Electrochem. Sci.*, 2008, **3**, 96–103.
27 P. Li, J. Deng, Y. Li, W. Liang, K. Wang, L. Kang, S. Zeng, S. Yin, Z. Zhao and X. Liu, *J. Alloys Compd.*, 2014, **590**, 318–323.
28 K. Hwang, B. Kang, S. Kim, S. Hwangbo and J. Kim, *Ceram. Int.*, 2012, **38**, S645–S647.
29 C. Sanchez, J. Livage, J. Audiere and A. Madi, *J. Non-Cryst. Solids*, 1984, **65**, 285–300.
30 W. Chen, J. Peng, L. Mai, H. Yu and Y. Qi, *Solid State Commun.*, 2004, **132**, 513–516.

31 A. Chu, M. Qin, B. Jia, H. Lu and X. Qu, *J. Am. Ceram. Soc.*, 2012, **95**, 2510–2515.

32 M. Huang, M. Qin, P. Chen, B. Jia, Z. Chen, R. Li, Z. Liu and X. Qu, *Ceram. Int.*, 2016, **42**, 10380–10388.

33 Y. Dong, M. Yu, Z. Wang, Y. Liu, X. Wang, Z. Zhao and J. Qiu, *Adv. Funct. Mater.*, 2016, **26**, 7590–7598.

34 X. Wang, Y. Zhang, C. Zhi, X. Wang, D. Tang, Y. Xu, Q. Weng, X. Jiang, M. Mitome and D. Golberg, *Nat. Commun.*, 2013, **4**, 2905.

35 M. Huang, M. Qin, D. Zhang, Y. Wang, Q. Wan, Q. He, B. Jia and X. Qu, *J. Alloys Compd.*, 2017, **695**, 1870–1877.

36 H. Wang, C. Zhang, Z. Liu, L. Wang, P. Han, H. Xu, K. Zhang, S. Dong, J. Yao and G. Cui, *Chem. Mater.*, 2011, **21**, 5430–5434.

37 L. Qie, W.-M. Chen, Z.-H. Wang, Q.-G. Shao, X. Li, L.-X. Yuan, X.-L. Hu, W.-X. Zhang and Y.-H. Huang, *Adv. Mater.*, 2012, **24**, 2047–2050.

38 M. Sathiya, A. Prakash, K. Ramesha, J. M. Tarascon and A. Shukla, *J. Am. Chem. Soc.*, 2011, **133**, 16291–16299.

39 Y. Shi, Z. Zhang, D. Wexler, S. Chou, J. Gao, H. D. Abruña, H. Li, H. Liu, Y. Wu and J. Wang, *J. Power Sources*, 2015, **275**, 392–398.

40 Z. Wang and L. Zhou, *Adv. Mater.*, 2012, **24**, 1903–1911.

41 X. Xu, R. Cao, S. Jeong and J. Cho, *Nano Lett.*, 2012, **12**, 4988–4991.

42 Y. Su, S. Li, D. Wu, F. Zhang, H. Liang, P. Gao, C. Cheng and X. Feng, *ACS Nano*, 2012, **6**, 8349–8356.

43 X. Sun, C. Zhou, M. Xie, T. Hu, H. Sun, G. Xin, G. Wang, S. M. George and J. Lian, *Chem. Commun.*, 2014, **50**, 10703–10706.

44 K. Chang, W. Chen, L. Ma, H. Li, H. Li, F. Huang, Z. Xu, Q. Zhang and J.-Y. Lee, *Chem. Mater.*, 2011, **21**, 6251–6257.

45 Y. Sun, X. Hu, W. Luo, F. Xia and Y. Huang, *Adv. Funct. Mater.*, 2013, **23**, 2436–2444.

46 V. Augustyn and B. Dunn, *Electrochim. Acta*, 2013, **88**, 530–535.

47 G. He, L. Li and A. Manthiram, *J. Mater. Chem. A*, 2015, **3**, 14750–14758.

48 C. Niu, M. Huang, P. Wang, J. Meng, X. Liu, X. Wang, K. Zhao, Y. Yu, Y. Wu and C. Lin, *Nano Res.*, 2016, **9**, 128–138.

49 J. M. Won, Y. N. Ko, J.-K. Lee and Y. C. Kang, *Electrochim. Acta*, 2015, **156**, 179–187.

50 J. T. Chen, K. Shin, J. M. Leiston-Belanger, M. Zhang and T. P. Russell, *Adv. Funct. Mater.*, 2006, **16**, 1476–1480.

51 W. Wang, J. Zhou, Z. Wang, L. Zhao, P. Li, Y. Yang, C. Yang, H. Huang and S. Guo, *Adv. Energy Mater.*, 2017, **8**, 1701648.

52 S.-H. Lee, V. Sridhar, J.-H. Jung, K. Karthikeyan, Y.-S. Lee, R. Mukherjee, N. Koratkar and I.-K. Oh, *ACS Nano*, 2013, **7**, 4242–4251.

53 S. Yin, Y. Zhang, J. Kong, C. Zou, C. M. Li, X. Lu, J. Ma, F. Y. C. Boey and X. Chen, *ACS Nano*, 2011, **5**, 3831–3838.

54 E. Kang, Y. S. Jung, G. H. Kim, J. Chun, U. Wiesner, A. C. Dillon, J. K. Kim and J. Lee, *Adv. Funct. Mater.*, 2011, **21**, 4349–4357.

55 A. D. Roberts, X. Li and H. Zhang, *Chem. Soc. Rev.*, 2014, **43**, 4341–4356.